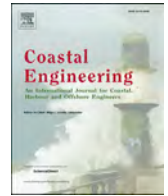


Contents lists available at [ScienceDirect](https://www.sciencedirect.com)

# Coastal Engineering

journal homepage: [www.elsevier.com/locate/coastaleng](http://www.elsevier.com/locate/coastaleng)

## Cross-shore variability and vorticity dynamics during wave breaking on a fixed bar

L. Chiapponi<sup>a</sup>, M. Cobos<sup>b</sup>, M.A. Losada<sup>b</sup>, S. Longo<sup>a,\*</sup><sup>a</sup> Dipartimento di Ingegneria e Architettura (DIA), Università di Parma, Parco Area delle Scienze, 181/A, 43124 Parma, Italy<sup>b</sup> Instituto Interuniversitario de Investigación del Sistema Tierra, Universidad de Granada, Avda. del Mediterráneo s/n, 18006 Granada, Spain

### ARTICLE INFO

#### Keywords:

Breaking waves  
Vorticity  
Laboratory experiments

### ABSTRACT

In the present experiments a volumetric particle-tracking system (V3V from TSI Inc.) allowed the measurement of the velocity fields generated by regular breaking waves past a fixed bar on a 1:10 rigid plane slope. The measurement volume extended from the wave crest to a portion of the domain below the wave trough, with two sets of monochromatic wave trains with different periods and heights. The aim of the present work is the quantification of the terms in the vorticity balance equation by including all the terms in a fully 3D approach. A possible new vorticity generation mechanism is revealed, that is amplified by the geometry of the laboratory flume and that awaits experimental validation in 3D wave tanks and in the field. The results are new and original and represent a data set for the comprehension of the effects of a submerged berm, for developing conceptual models of vorticity and for the calibration of numerical codes.

### 1. Introduction

Breaking waves in shallow water are the most prominent feature of the flow field in the nearshore and in the surf-zone and affect sediment transport and the bottom shape of sandy beaches either directly or indirectly through the generated currents. They generate ample vorticity often in presence of preexisting vorticity due to the past sequence of bores. The mechanism is strongly influenced by the geometry of the bottom, which is often characterized by single or multiple bars. Bars are an important feature of many natural beaches. The seminal paper by Roelvink and Stive (1989) lists numerous models invoked to explain the observed patterns of bars, and the contributions to their generation due to asymmetric oscillatory flow, long-wave flow generated by wave grouping, turbulent flow due to breaking, undertow due to momentum decay, mass and momentum transport (see Baldock et al., 2004; Baldock, 2006). Field observations of the bars indicate that they are related to reflecting free long waves, eventually in the presence of leaky waves or edge waves. The bars, in turn, modify the flow pattern and induce refraction, diffraction, reflection of the wave energy offshore, and affect the rip currents position. In this respect there are many differences of all

the wave characteristics if a bar is present or absent, in the regime of sediment transport, of the currents, in all the main complex features that finally control the short and the long-term evolution of the beach. A detailed 3D experimental analysis of the effects of the bars with rip channels is reported in Haller et al. (2002). As a consequence, the knowledge of these modifications induced by the bars helps in planning the artificial berms and in analyzing their effects. The specific geometry of the present experiments, with a submerged bar mimicking a sand bar present in natural cross-shore sections of beaches, makes the analysis applicable. The detailed analysis of momentum balance and turbulence can be found in Clavero et al. (2016), in the present analysis we are mainly interested in vorticity structure and balance. Vorticity generation in dissipating and breaking waves is widespread in numerous geophysical phenomena, in the sea and in the atmosphere (see, e.g., Holton et al., 1995). Usually, a link can be detected and quantified between the energy decay or the momentum decay of waves and vorticity creation, which can be used for limiting the computation efforts in modeling large scale phenomena (Bühler, 2000).

Vorticity in the nearshore is generated at two different length scales, (i) at the scale of the crest length (large scale), and (ii) at the scale of the

\* Corresponding author.

E-mail address: [sandro.longo@unipr.it](mailto:sandro.longo@unipr.it) (S. Longo).

<http://dx.doi.org/10.1016/j.coastaleng.2017.06.011>

Received 30 July 2016; Received in revised form 31 March 2017; Accepted 2 June 2017

wave crest (small scale). The vorticity at the scale of the crest length is mainly represented by eddies with vertical axis and has important implications in the shape of the breaker and in the morphodynamics of the submerged beach. See [Peregrine \(1998\)](#) for the description of the surf zone currents and for several insights of the processes related to vorticity in the surf zone.

The vorticity at the scale of the wave crest (small scale) is more amenable to experimental analysis in the lab and again has a quite important role in wave breaking and post-breaking development. We first note that vorticity (it is true also at large scale) is not merely a different point of view of the flow field by analyzing the curl of the velocity, but offers new insights in complex flow fields where momentum, energy, chemicals, can be efficiently trapped in eddies or other coherent structures. In this respect, the oblique descending eddies and the multiple horizontal eddies (parallel to the wave crest) observed and documented by [Nadaoka et al. \(1989\)](#), increase the mass and momentum transport and favors a decrease in wave height. The video image analysis in the experiments by [Zhang and Sunamura \(1994\)](#) confirmed the role of the breaker-induced vortices in multiple bar formation.

The source of vorticity in breaking waves has been explained in different ways (see [Longo et al., 2002](#) and references therein). The most obvious source is at the bottom, but we neglect it since it has a modest intensity and a marginal role during breaking and we will consider only other regions of generation of vorticity, mainly the region beneath the free surface. [Longuet-Higgins \(1992\)](#) explained the appearance of vorticity in the waves in terms of the combined effects of surface curvature and zero-shear stress boundary conditions at the interface, with a Stokes layer initially confining the generated vorticity, which in a subsequent stage escapes and fills the domain. [Yeh \(1991\)](#) considered the baroclinic torque in the presence of a density gradient to be the main driver of vorticity generation, with the viscous-shear torque of negligible relevance. The free surface fluid deceleration before breaking (with an increase of fluid pressure on the back of the wave, pushing the crest to spill or to plunge) is considered a major source of vorticity in spilling breakers by [Dabiri and Gharib \(1997\)](#), in contrast with previous studies attributing the vorticity generation to the sharp curvature of the interface, where a flow separation occurs ([Lin and Rockwell, 1994](#)).

The various phenomena occurring after vorticity generation in breaking waves have been numerically analysed in [Watanabe et al. \(2005\)](#). All the analyses agree that there is a continuous generation of vorticity at the front of the breaker that appears similar to a comet, with a core moving with the crest and the tail spreading out behind the crest (e.g., [Lin and Liu, 1998](#)). In most (if not all) cases, this vorticity is coupled with turbulence.

Early measurements of vorticity using planar Particle Image Velocimetry (PIV) were obtained by [Petti et al. \(1994\)](#), who made experiments with waves breaking on a submerged breakwater on 1:100 beach, and by [Chang and Liu \(1998\)](#), who gained information on the overall characteristics of the (two-dimensional) flow field of breaking waves in shallow water and confirmed the existence of oblique vortices. An extensive investigation on surf-zone breaking waves over a sloping beach with PIV is reported in [Kimmoun and Branger \(2007\)](#), including the longshore vorticity measurement. The mean vorticity dynamics under breaking waves has been numerically analysed, amongst numerous authors, by [Lin and Liu \(1998\)](#) in a two-dimensional framework, where vortex stretching is absent and only advection and diffusion redistribute the vorticity once it has been generated. A large eddy simulation of breaking waves in a 3D domain has been performed by [Christensen and Deigaard \(2001\)](#) for spilling, plunging and weak plunging waves. However, to the best of our knowledge, no experimental data on three-dimensional vorticity structure and dynamics have yet been presented and discussed, with the exception of the recent paper by [Ting and Reimnitz \(2015\)](#) who focused on coherent structures in a

breaker on an inclined bottom (in different flow fields, vorticity analysis of experimental data obtained with a system identical to the V3V system of the present experiments has been documented in [Calderon et al., 2012](#)). A key element of the analysis is that vorticity dynamics is a 3D phenomenon which can be properly modeled or described only having the three components of velocity in space. Given the inherent three-dimensional structure of the breaking waves and the relevance of stretching processes, a step forward is necessary to fill this gap in knowledge. This step is allowed by the new measurement system represented by the three-dimensional particle tracking device adopted in the present experiments. The availability of instantaneous velocity measurements with a decent spatial resolution and data rate, allow the computation of virtually all the terms and variables (with the exception of pressure) in the equations of the most adopted models, hence allow some kinds of analyses never attempted in the past (or conducted with a series of approximations and simplifying hypotheses).

The aims of the present work are the analysis and balance of vorticity at the wave crest scale in the presence of a bar. The results are compared to vorticity measurements in similar conditions but without bar, in order to estimate the differences.

The experimental layout and the experiments and the data analysis are detailed in [Clavero et al. \(2016\)](#) and are briefly described in the present work in §2 and in §3. Section 4 describes the structure of the vorticity with quantification of the balance of vorticity. A possible new mechanism for vortex generation at the free surface is discussed in §5. The conclusions are reported in §6.

## 2. Experimental set-up and experiments

The experiments were conducted in the wave flume located in the Laboratorio de Dinámica de Fluidos Ambientales of the CEAMA (Centro Andaluz de Medio Ambiente) in Granada, with an artificial slope of 1:10 and with a berm of stones and plastic blocks, see [Fig. 1](#). The flume is 23 m long and 65 cm wide. The still-water depth in front of the paddle was of 43 cm and an active absorption system (AWACS) was active during the experiments.

Velocity measurements were taken with a 3D Particle Tracking Velocimetry system (V3V from TSI Inc.) in a volume of measurements with a side length equal to  $\approx 14$  cm in the cross-shore and vertical directions and equal to  $\approx 10$  cm in the alongshore direction. It was centred at  $X = 1138$  cm in the mid section of the flume, with a minimum distance of the measurements  $\approx 25$  cm from the side walls. In this condition the side walls effects can be safely assumed as negligible. The volume of measurement was illuminated by a laser and three cameras ( $2048 \times 2048$  pixels) generated three pairs of 12-bit images. The two images of each pair were captured with a time delay of  $100 \mu\text{s}$ . The surface elevation during tests was measured in several sections (see [Fig. 1a](#)), including the section of the breaker, using Ultrasonic probes (UltraLab<sup>®</sup> USL 80D by General Acoustics, sensor model USS635, with an accuracy on the instantaneous water level measurements equal to  $\pm 0.5$  mm). The acquisition of the V3V images was triggered by the water level measured in Section 4, at the internal toe of the bar: the firing of the laser was corresponding (with a delay) to the maximum of the water surface elevation. Due to the intrinsic random nature of the breaking waves and to the uncertain definition of “maximum”, a fluctuation of less than 0.02 s was recorded for the 10 sequences of shots. The images were post-processed in order to detect the ‘triplets’ of particles (a triplet indicates the same particle observed by the three cameras) in two subsequent images. Then the calibration of the cameras allowed the computation of the spatial coordinates of the particles in time, and of the three components of the velocity of the particles, subject to further validation (see [Ohm and Li, 2000](#) and [Sharp et al., 2010](#) for details on the procedures and on the algorithms). In the best shots we had images containing  $\approx 100\,000$  particles with more than

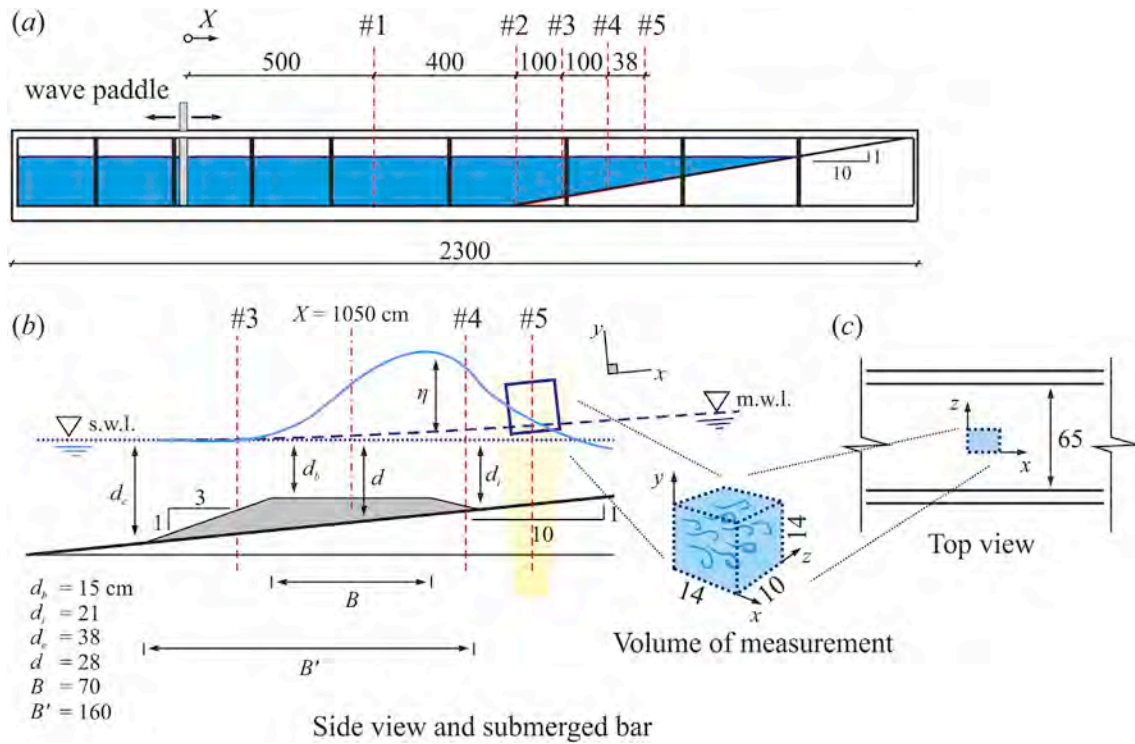


Fig. 1. The experimental flume adopted for the tests: (a) side view of the flume; (b) the geometry of the bar, with  $d_b/d = 0.54$ , where  $d = 28$  cm is the still water depth in the mid section of the bar ( $X = 1050$  cm); (c) top view. The flume is 23 m long and 65 cm wide and the minimum size of the volume of measurement (10 cm) is in the alongshore direction. The dot line indicates the still water level, the dashed line is the mean water level  $\bar{\eta}$  (wave set-up or set-down). Dimensions are in centimeters.

25 000 validated particle velocities. That means approximately 1 particle velocity for each cell of a regular grid with a step of 0.4 cm. As for the accuracy of V3V and of the algorithms, we can use the results by Ting and Reimnitz (2015), who used an identical system in similar flow conditions: 0.1 cm/s for the cross-shore and the vertical direction, and 0.4 cm/s for the alongshore velocity component. The accuracy in turbulence velocity and kinetic energy was  $\approx 10\%$  and  $\approx 20\%$ , respectively (turbulence velocities of the order of  $\approx 50$  cm/s and turbulent kinetic energy (TKE) of the order of  $\approx 10^3$  cm<sup>2</sup>/s<sup>2</sup>). The frequency of V3V was 7.25 Hz, with 10 and 13 shots per each period for waves with  $T = 1.5$ , 2.0 s, respectively. Each experiments contained 10 cycles, with a total of 100 and 130 shots.

The uncertainty in vorticity estimation can be evaluated as follow (see also Longo et al., 2014; Raffel et al., 2013). The spatial derivatives were calculated with a central scheme with uncertainty  $\epsilon_{\partial u_i / \partial x} = \pm 0.7 \epsilon_u / \Delta x$ , with  $\epsilon_u$  the uncertainty in measuring the fluid velocity and  $\Delta x$  the space increment in the derivatives. The uncertainty in the vorticity is the sum of the uncertainties of the two derivatives and is maximum for the components  $\omega_z$  and  $\omega_x$ , with  $\epsilon_{\omega_x} = \epsilon_{\omega_z} = 0.9$  s<sup>-1</sup>, is minimum for the component  $\omega_y$ , with  $\epsilon_{\omega_y} = 0.4$  s<sup>-1</sup>. The vertical profiles of vorticity are the average of  $N \approx 8000$  profiles, hence the uncertainty of the averaged values is reduced. The reduction factor is different if the profiles are considered (i) uncorrelated, and (ii) partially correlated. In case (i) the reduction factor would be  $\sqrt{N} \approx 90$ ; in case (ii) the number of equivalent uncorrelated observations  $N_e$  is (Kowalczyk et al., 2012)

$$N_e = N \frac{1 - \rho_l}{1 + \rho_l}, \quad (1)$$

where  $0 < \rho_l < 1$  is the correlation parameter between the data series. We expect that vertical profiles captured within the same shot are correlated, whereas vertical profiles belonging to different wave cycles (for the same phase) are uncorrelated. Hence, the sample size is equal to the number of

profiles for each shot,  $N_p \approx 800$ . An estimate of the correlation parameter  $\rho_l$  is quite difficult and involves the complete description of the vorticity flow field. With a pragmatic approach, by assuming that  $\rho_l = 0.9$  (very high correlation), results  $N_e \approx N_p / 20 \approx 40$ . Further averaging the 10 cycles, results in a reduction factor  $\sqrt{10} \times 40 = 20$ .

Within this framework of statistical analysis, the uncertainties of the averages are  $\epsilon_{\bar{\omega}_x} = \epsilon_{\bar{\omega}_z} = 0.05$  s<sup>-1</sup> and  $\epsilon_{\bar{\omega}_y} = 0.02$  s<sup>-1</sup>. Upon the introduction of a time scale  $\sqrt{(d + \bar{\eta})/g}$ , the dimensionless uncertainties are  $\epsilon_{\bar{\omega}_x} = \epsilon_{\bar{\omega}_z} = 7 \cdot 10^{-3}$  and  $\epsilon_{\bar{\omega}_y} = 3 \cdot 10^{-3}$ , respectively.

The main parameters of the experiments are listed in Table 1.

All the experiments have been set-up in order to reduce at a minimum the air (Clavero et al., 2016). This is also confirmed by the sequence of images taken with the V3V system, where no scattering due to air bubbles can be detected. The presence of air bubbles would require a different approach with a two-phase analysis (see, e.g., Derakhti and Kirby, 2014). The list of the experiments has been presented for completeness, but the detailed analysis of vorticity will be limited to Experiment 9, with few other references to Experiment 6. Some preliminary evaluations on the whole set of experiments revealed that the differences amongst the 9 experiments were not so relevant to deserve a more detailed analysis.

### 3. Data analysis and visualization

The time series was treated by applying averages of different kinds. We define the phase-average for the variable  $a$  as

$$\bar{a}(t) = \frac{\sum_{i=1}^{N_c} a(t + iT)}{N_c}, \quad 0 < t \leq T, \quad (2)$$

where  $T$  is the period of the signal and  $N_c$  is the number of cycles. The time-average is defined as

**Table 1**

Parameters of the tests.  $H_0$  is the target wave height (almost coincident with the generated wave height),  $T$  is the period and  $H_0/L_0$  is the deep-water wave steepness.  $\xi_0 = \tan\alpha/\sqrt{H_0/L_0}$  is the Iribarren number ( $\alpha$  is the bed slope),  $h = d + \bar{\eta}$  is the mean water depth in the section of measurements,  $\bar{\eta}$  is the wave set-up, and  $H_{b-rms}$ ,  $H_{b-1/3}$ , and  $H_{b-max}$  are the root-mean-square wave height, the mean of the highest third of the waves, and the maximum wave height, respectively, all referred to as the statistics of the breakers.  $d_i$  and  $d_e$  are the still-water depth at the internal and external toe of the bar, respectively,  $B$  and  $B'$  are the width of the crest and the total width of the bar. The still-water depth in front of the paddle is 43 cm and the breaking section is #5 at  $X \approx 1138$  cm, with a still-water depth  $d = 19.2$  cm.

Exp.	$H_0$ (cm)	$T$ (s)	$H_0/L_0$	$\xi_0$	$h$ (cm)	$\bar{\eta}$ (cm)	$H_{b-rms}$ (cm)	$H_{b-1/3}$ (cm)	$H_{b-max}$ (cm)	$d_i/L_0$	$d_e/L_0$	$B/L_0$	$B'/L_0$
1b	6	1.5	0.017	0.765	19.2	0.0	5.7	6.2	6.3	0.060	0.109	0.199	0.456
2b	7	1.5	0.020	0.708	19.4	0.2	7.4	8.1	8.7				
3b	8	1.5	0.023	0.662	19.6	0.4	8.0	8.6	8.8				
4b	9	1.5	0.026	0.624	19.7	0.5	8.7	9.2	9.9				
5b	10	1.5	0.028	0.592	19.8	0.6	9.2	9.9	10.4				
6b	6	2	0.010	1.020	19.4	0.2	6.1	6.3	6.5	0.034	0.061	0.112	0.256
7b	7	2	0.011	0.944	19.4	0.2	7.6	8.3	8.7				
8b	8	2	0.013	0.883	19.5	0.3	9.0	9.6	10.4				
9b	9	2	0.014	0.833	19.6	0.4	10.3	11.2	12.8				

$$\bar{a} = \frac{\sum^N a}{N}, \tag{3}$$

where  $N$  is the number of elements of the sample, and the (time-)phasic-average is defined as

$$\langle a \rangle = \frac{\sum^N a\phi}{\sum^N \phi}, \tag{4}$$

where  $\phi = 1$  and  $\phi = 0$  if water is present or absent, respectively. The water local fraction is  $\alpha = \sum \phi/N$  and  $\alpha = 1$  below the (minimum) trough level, and  $\alpha = 0$  above the (maximum) crest level. The phasic-average is always greater than and equal to the time average if  $\alpha < 1$  and  $\alpha = 1$ , respectively.

The phasic-phase-average is also defined as

$$\langle \tilde{a}(t) \rangle = \frac{\sum_{i=1}^{N_c} a(t+iT)\phi(t+iT)}{\sum_{i=1}^{N_c} \phi(t+iT)}, \quad 0 < t \leq T, \tag{5}$$

by applying the phase-average and the phasic-average operators simultaneously. In the present analysis we will show in the figures ‘vertically integrated’ data, meaning data phasic-averaged in the vertical, and ‘cycle integrated’ equivalent to a time-average or a phasic-average according to the indications. Figures and diagrams have the time (or phase) horizontal axis in descending values for a better interpretation of the data.

Fig. 2 shows the shape of the wave at the breaking section for all the experiments.

The methodology adopted to separate periodic components and fluctuating components is detailed in Clavero et al. (2016). First (i) a principal orthogonal decomposition (POD) is applied to the time series of the spatial measured velocity in order to detect the most energetic contributions; (ii) then a cut-off number of components is chosen in order to eliminate disturbances and the reconstructed time series with a limited number of modes is used (iii) to analyze vorticity balance. The results are presented as average in the cross-shore and alongshore directions, obtaining a single profile in the vertical per shot as average of  $\approx 800$  profiles. When the results are further phase

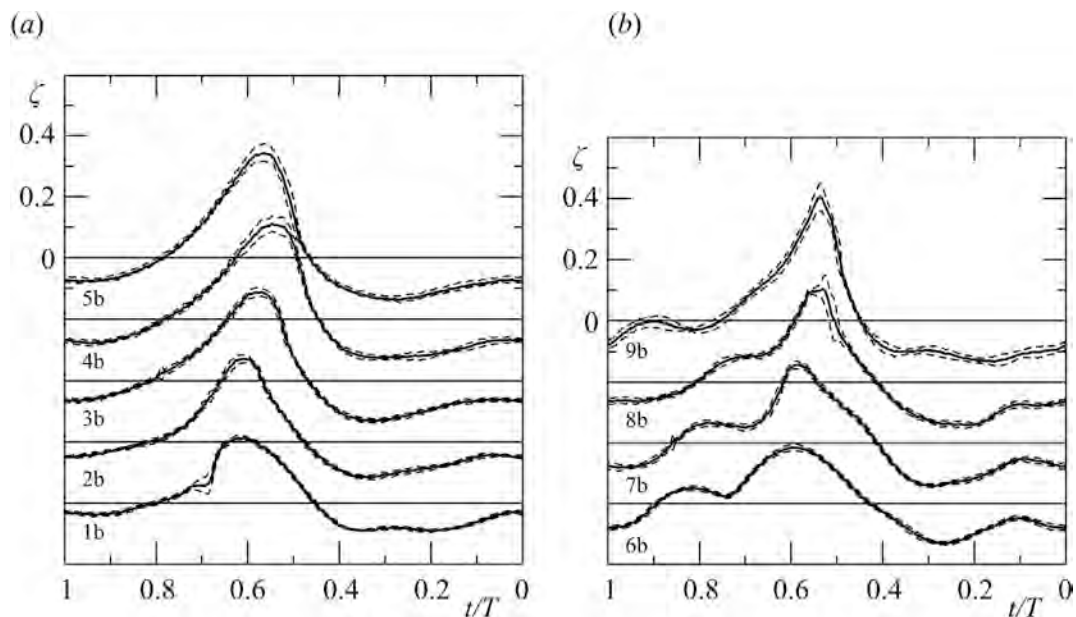


**Fig. 2.** Phase-averaged surface elevation at the section of velocity measurements (Section 5) for (a) the tests with  $T = 1.5$  s, and (b) the tests with  $T = 2.0$  s. The dashed lines limit the  $\pm 1$  standard deviation band for the sample of 10 wave cycles during velocity acquisition.

averaged over 10 cycles, each profile in the vertical is the average of  $\approx 8000$  profiles, by far more than in most other experiments on breaking waves. Some convergence tests detailed in Clavero et al. (2016) indicate that the mean velocity computed with  $\approx 300$  profiles is almost coincident with the mean velocity obtained by averaging  $\approx 8000$  profiles, with an average relative error of  $\approx 0.6\%$ . The rate of convergence is slower for the turbulent kinetic energy, showing a relative error of  $\approx 6.5\%$ .

Most of the results are presented in non-dimensional form with a vertical length scale given by the mean water depth  $d + \bar{\eta}$ , where  $d$  is the still-water depth and  $\bar{\eta}$  is the time-averaged surface elevation. The velocity scale is given by  $\sqrt{g(d + \bar{\eta})}$ , and the time scale is given by  $\sqrt{(d + \bar{\eta})/g}$  (this scale is commonly used instead of the wave period  $T$ ). Surface elevations are measured from the mean water level,  $\zeta = (y - \bar{\eta})/(d + \bar{\eta})$ .

Figure Appendix A.1 in Appendix shows the instantaneous velocity vectors (only cross-shore and vertical components) for Experiment 6b, phase 4, first wave cycle. The panels refer to different values of  $z$  and are 0.8 cm apart.

#### 4. Vorticity analysis

##### 4.1. A qualitative analysis of vorticity

The vorticity in breaking waves shows many complex features due to the intrinsic non-stationarity of the flow field and has an evident three-dimensional structure. In Fig. 3ab the pattern described in Zhang and Sunamura (1994) is shown for spilling and plunging breakers, respectively, with oblique vortices and horizontal vortices. For spilling breakers the excess of surface pressure plus turbulence generate oblique injection, related with the front advance. For plunging breakers the local jet impinging the surface creates rotating fluid with horizontal axes washing the oblique jets. Fig. 3c shows a possible pattern if a submerged berm is present, with horizontal and inclined vortices coexisting. It is the same pattern described in Zhang and Sunamura (1994) for spilling-plunging breakers, a hybrid between horizontal and oblique vortices. Rollers and vortices of various shapes fill the fluid domain in the presence of breaking waves and are a key element in the interpretation of the free surface shape and the abrupt changes in fluid motion. The presence of overturning jets meeting the

water domain ahead of the wave induces instability to the turbulent flow field and triggers a three-dimensional evolution of the entire flow field. If two subsequent spanwise (alongshore) vortices are generated by the breaking process, the vortex filaments lying between these vortices are perturbed and stretched, evolving in a sequence of counter-rotating streamwise (cross-shore) vortices. These streamwise vortices generally (but not in all circumstances) evolve into obliquely descending eddies, first observed by Nadaoka et al. (1989). Fig. 4 shows three frames taken with a Photron SA3 fast camera at 2000 frames/s. The images feature an oblique eddy that moves following the fluid. A video, available as Supplementary Material, shows the persistent structure of the eddy and its rotation as its axis translates and tilts slightly. In order to visualize the vortices the parameters of the waves for this specific photos were chosen to favor air bubbles entrainment during breaking, whereas attention was paid to avoid bubbles during V3V acquisition.

Supplementary video related to this article can be found at <http://dx.doi.org/10.1016/j.coastaleng.2017.06.011>.

Other different phenomena can generate eddies. For instance, the velocity profile for undertow has a shape that triggers instabilities evolving in spanwise (alongshore) large eddies that move offshore (Li and Dalrymple, 1998). All these eddies have a major role in the initial stage of the cascade mechanism of turbulence.

A view of the complex experimental vorticity field is obtained through a visualization of the vorticity tubes, whose axes are coincident with the vortical lines and cross sections are proportional to the local vorticity magnitude. Fig. 5a shows the vortical tubes for Experiment 6b, phase 4, during the first measured wave cycle. The seeding points for tracing the vortical tubes are distributed in the vertical planes at the entry and exit sections. Numerous loops are present in these vortices, and they resemble ring vortices stretched along the axis of symmetry and merging with the neighbouring vorticity. A more complex pattern of vorticity tubes is evident for Experiment 9b, phase 7 in Fig. 5b. The vorticity tubes are widely studied since their geometry and evolution is a mirror of the overall organization of the flow (see, e.g., Fritts et al., 1998 for a discussion of vorticity tubes in breaking internal gravity waves). The tubes appear as wrapping around other coherent structures and are an experimental confirmation of the complex scenario. The evolution is quite different if the tubes are initially parallel or orthogonal; a single tube can unravel into two intertwined separate tubes, eventually bursting or

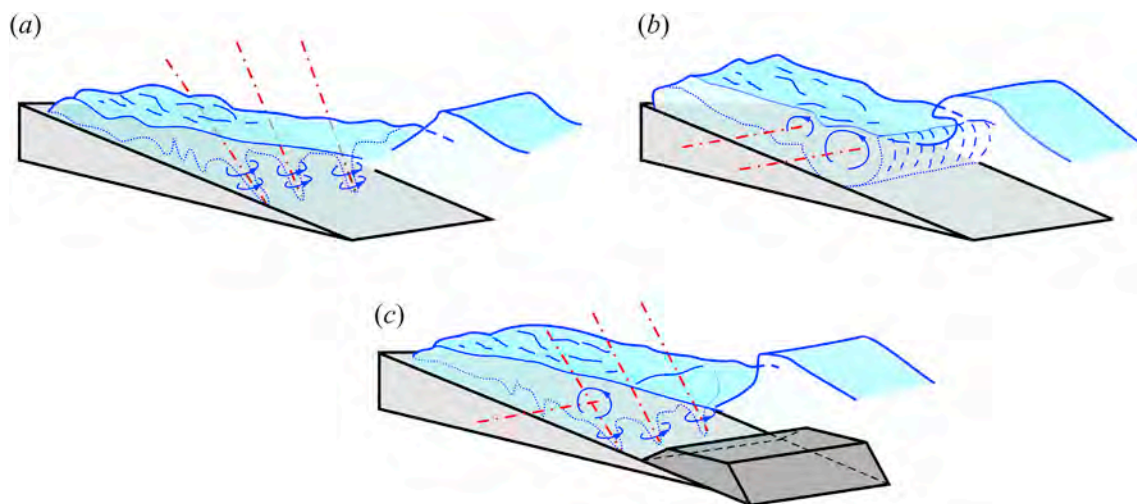


Fig. 3. Vortex types for (a) spilling breakers; (b) plunging breakers; (c) breakers on a submerged berm. The dashdot lines indicate the axis of the vortices, the dashed curves limit the domain with high turbulence and possibly with air bubbles (modified from Zhang and Sunamura, 1994).

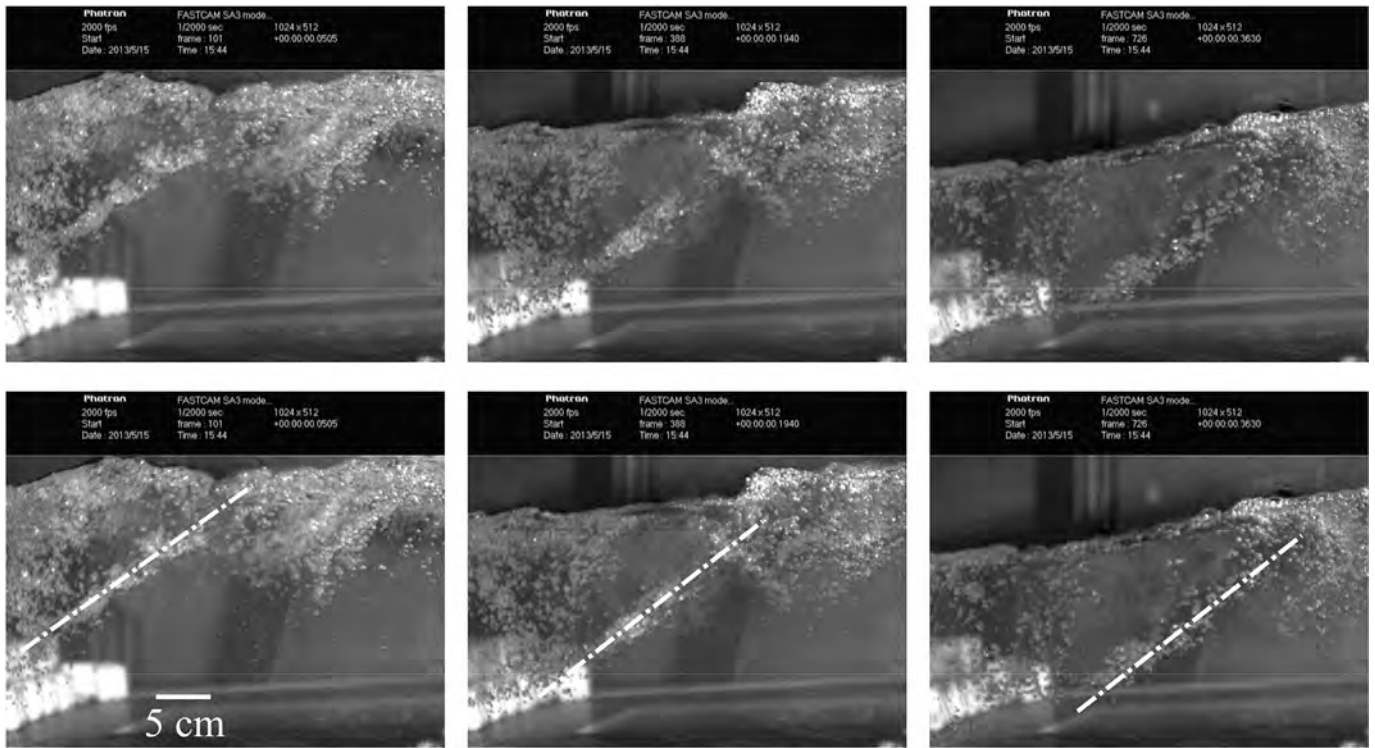


Fig. 4. An oblique diagonal vortex. The lower panels show the axis of the eddy, advected by the mean flow and with the axis slightly tilting. The three images have been acquired with a fast camera at 2000 frames/s and show the breaker evolution at various times  $\approx 0.15$  s apart. The bar is visible on the left and the glass window for laser enlightening from below is visible at the bottom.

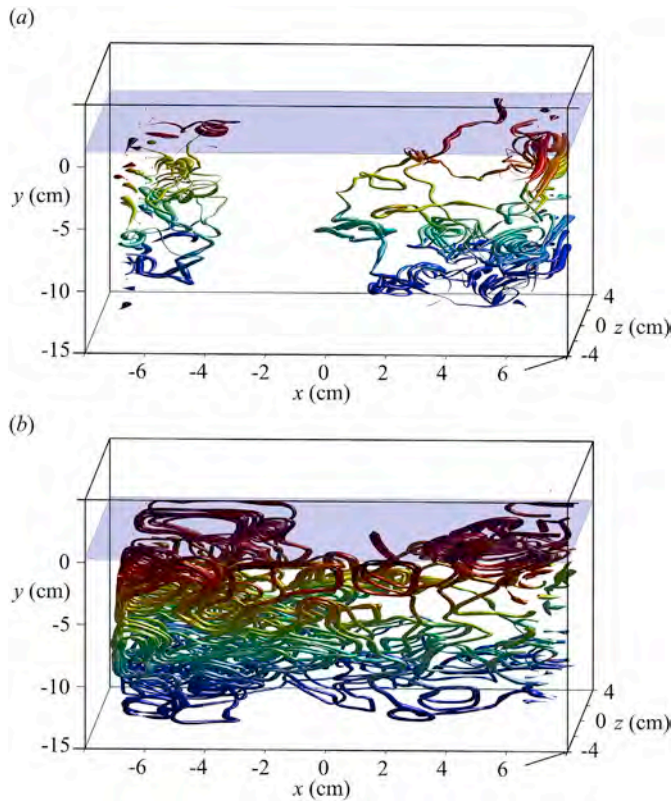


Fig. 5. Vorticity tubes for (a) Experiment 6b, fourth phase, first wave cycle, (b) Experiment 9b, seventh phase, first wave cycle. Different colors indicate the vertical location of the tubes. The shadowed horizontal plane indicates the free surface level. (For interpretation of the references to colour in this figure legend, the reader is referred to the web version of this article.)

fragmenting. All this ‘ballet’ of vorticity tubes transfer energy and enstrophy toward smaller length scale and is likely to be representative of turbulent transition in many flows.

A classical view of the vorticity field with slices of the volume of measurements is shown in Figure Appendix A.2abc in the Appendix, in which the magnitude of the three components of instantaneous vorticity, with streamlines and vorticity lines, is drawn for the same data shown in Fig. 5a.

#### 4.2. A quantitative analysis of vorticity

The variables in the turbulent flow are separated into an (phase-) average value and the fluctuation:

$$u_i = \tilde{u}_i + u'_i, \quad \omega = \tilde{\omega} + \omega', \quad (6)$$

where  $i = 1, 2, 3$ , with  $u_1 = u$ ,  $u_2 = v$ , and  $u_3 = w$  indicating the three components of velocity in the orthogonal Cartesian system  $x - y - z$ ,  $\omega_i = \epsilon_{ijk} u_{k,j}$  ( $\epsilon_{ijk}$  is the alternating Ricci's tensor). The phase-averaged velocity  $\tilde{u}_i$  is the organised part of the flow and in the present analysis includes the time-averaged velocity (the undertow below the trough level). Hereafter, a repeated index indicates summation unless otherwise stated.

The equation for the mean vorticity is obtained by applying the operator curl to the Navier-Stokes equation, resulting in the following expression (e.g., Tennekes and Lumley, 1972):

$$\underbrace{\frac{\partial \tilde{\omega}_i}{\partial t}}_{I_v} + \underbrace{\tilde{u}_j \frac{\partial \tilde{\omega}_i}{\partial x_j}}_{II_v} = - \underbrace{\frac{\partial}{\partial x_j} \left( \tilde{u}'_j \omega'_i \right)}_{III_v} + \underbrace{\tilde{\omega}'_j \tilde{S}'_{ij}}_{IV_v} + \underbrace{\tilde{\omega}_j \tilde{S}'_{ij}}_{V_v} + \underbrace{\nu \frac{\partial^2 \tilde{\omega}_i}{\partial x_j \partial x_j}}_{VI_v}, \quad (7)$$

where  $S_{ij} = 1/2(u_{i,j} + u_{j,i})$  is the rate of strain tensor and  $\nu$  is the kinematic viscosity of the fluid. The two terms  $I_v$  and  $II_v$  have obvious meaning, the term  $III_v$  is the mean transport of the fluctuating vorticity due to the

fluctuating velocity, the terms  $IV_v$  and  $V_v$  are vortex stretching terms, which are key elements for transferring energy from the large scale to the small scale arising in a three-dimensional approach to vorticity dynamics. In particular, the term  $\overline{\omega'_j S'_{ij}}$  is a gain or a loss of the mean vorticity due to the coupling between fluctuating vorticity and stretching induced by turbulence. The term  $VI_v$  is the viscous dissipation of the mean vorticity.

Fig. 6abc shows the non-dimensional cross-shore, vertical and alongshore vorticity for Experiment 9b. Fig. 6d shows the phase-averaged surface elevation and the instant of shooting of the V3V system. Crest and trough are located at  $\zeta = 0.43$  and  $\zeta = -0.11$ , respectively, and the vertical extension of the FOV is between  $\zeta \approx 0.31$  and  $\zeta \approx -0.42$ . Phases 1 and 2 are across the crest and only a small part of the crest is missing from the data analysis. However, the peak values are missing because no phase is perfectly coincident with the crest of the breaker.

The most important component is the alongshore vorticity, mainly negative and with higher values in the crest. Comparing these results with the vorticity distribution (after scaling) depicted in Fig. 4 in Longo (2003), we note that the vorticity is more uniformly distributed in the vertical and of minor intensity. It is partly a consequence of the berm presence that helps in developing vorticity also at the berm edge, not only

near the free surface. There is a slowly varying depth, an abrupt change and an almost constant depth during the development of the vorticity. It is also due to the different technique of fluid velocity measurements, a Laser Doppler in Longo (2003) with a huge data rate with respect to the data rate of the present experiments. Finally, a frozen turbulence hypothesis was used in Longo (2003) to transform the time gradient of the measured velocity into space gradients needed for vorticity evaluation, whereas a direct estimation of space gradients is performed with the present V3V data. A more detailed comparison with other experimental data is reported in §4.3.

The available data allow the computation of all the terms in eq. (7). Fig. 7abc shows the phase-averaged vorticity in the three directions - cross-shore, vertical and alongshore - for Experiment 9b. The interpretation is made easy by observing the values averaged in the vertical direction, as shown in Fig. 7d. Before breaking (phase 1), the cross-shore and the alongshore vorticity components are positive, with a vertical vorticity of almost zero. After breaking (phase 2), the cross-shore vorticity decreases and oscillates around zero, the vertical vorticity becomes negative and achieves its maximum negative value, assuming in subsequent phases a positive value. The vectors in the upper part of panel d illustrate the average vorticity in the  $x-y$  plane in different phases and

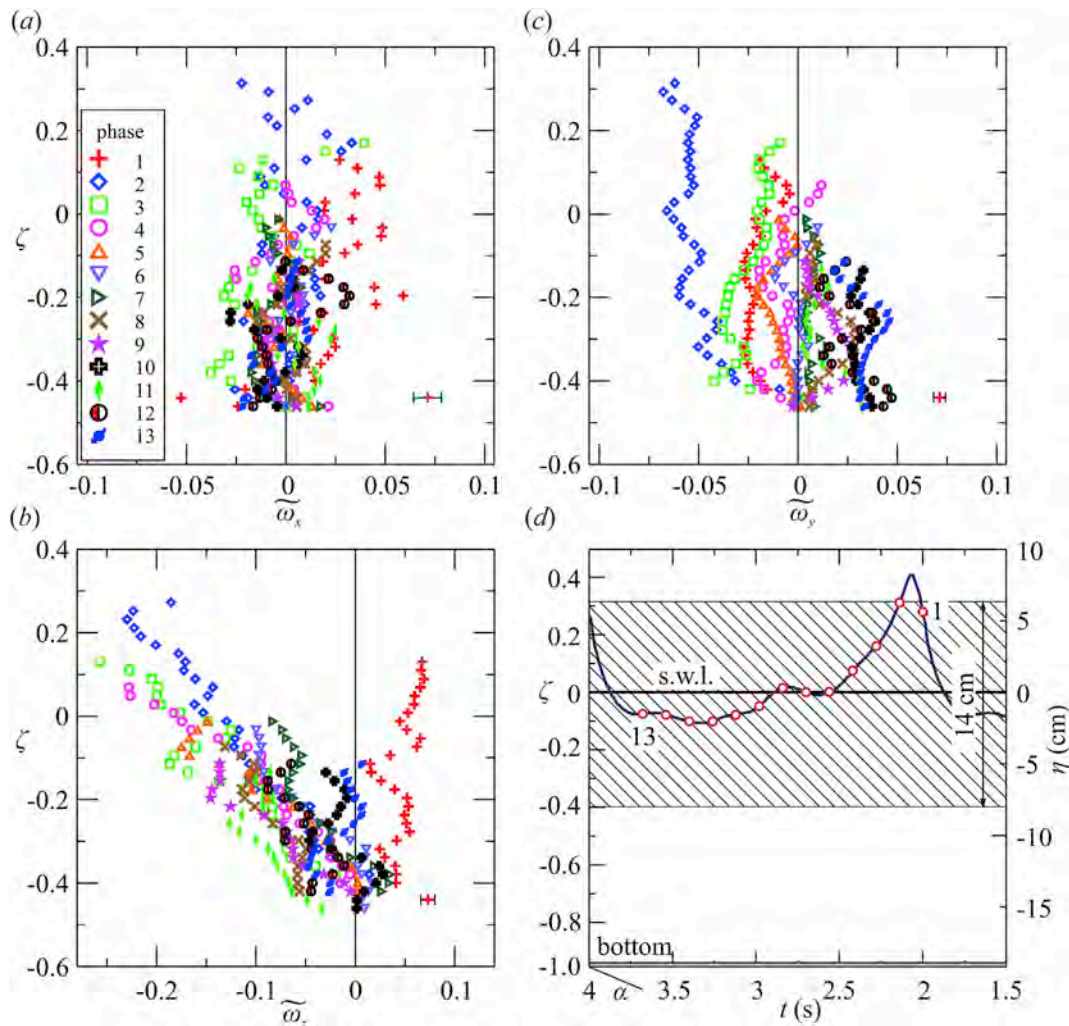
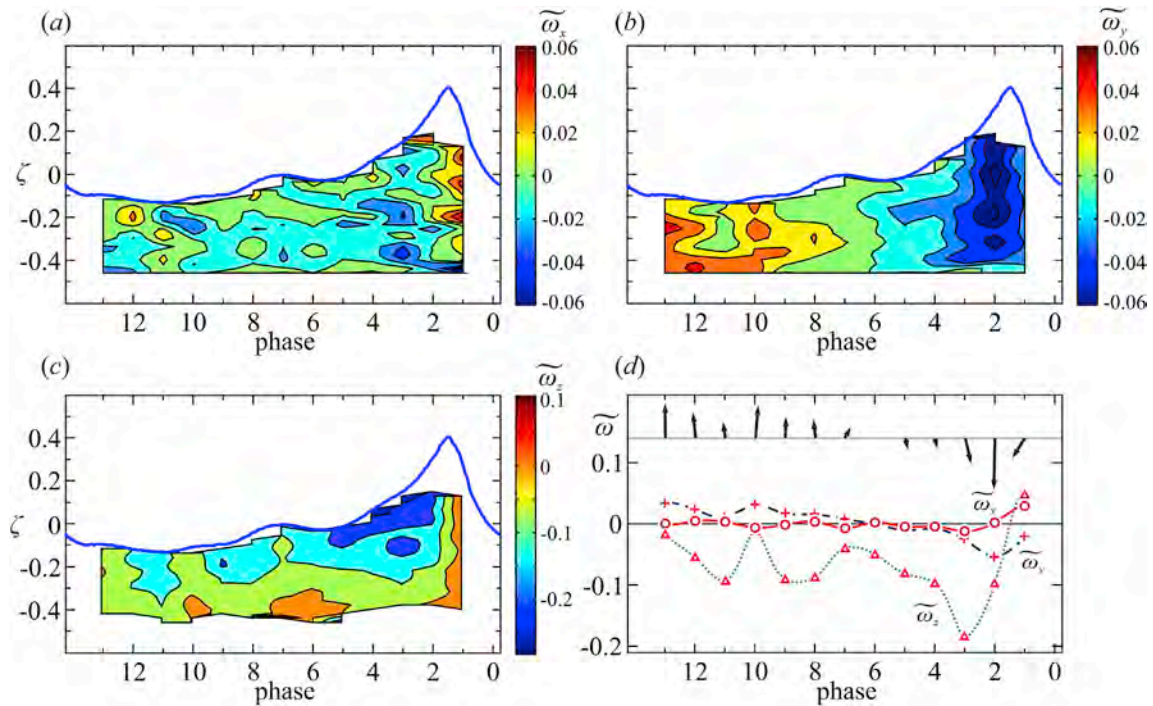


Fig. 6. Experiment 9b. (a) Phase averaged cross-shore vorticity, (b) vertical vorticity, and (c) alongshore vorticity as a function of  $\zeta = (y - \bar{\eta}) / (d + \bar{\eta})$ . (d) Phase-averaged surface elevation with symbols indicating the 13 phases of measurements. The hatched area indicates the FOV of the V3V system. The vorticity is normalized by  $\overline{\omega} \sqrt{(d + \bar{\eta})} / g$ . Error bars refer to one standard deviation.



**Fig. 7.** Experiment 9b. (a) Phase resolved cross-shore vorticity, (b) vertical vorticity, and (c) alongshore vorticity as a function of  $\zeta = (y - \bar{y}) / (d + \bar{y})$ . (d) Mean values in the vertical of the cross-shore (circles), vertical (crosses), and alongshore (triangles) vorticity, with the vectors representing the magnitude and orientation of the average  $x-z$  components of vorticity. The vorticity is normalized by  $\bar{\omega} \sqrt{(d + \bar{y}) / g}$ .

can be considered representative of the axis of the vertical or inclined eddies (however, high levels of vorticity can also be attributed to shear and not to coherent structures). The vectors are subject to a clock-wise rotation of the axis of the eddies occurs after breaking and resembles the experimental observations of, for example, [Nadaoka et al. \(1989\)](#). Vortex stretching occurs, with the axis of the vortices aligned with one of the principal axes of strain.

The alongshore vorticity ([Fig. 7c](#)) is the component most influenced by the breaker. Near the surface, a strong negative value of the alongshore vorticity is observed, coherent with the clock-wise rotation (as observed with a side view with the paddle on the left and the shore on the right) generated by the overturning crest, which spreads to the rear of the breaking front. [Fig. 7d](#) shows the evolution of vorticity in a different phase, with values integrated in the vertical. The alongshore vorticity component (triangles connected by a dotted line in [Fig. 7d](#)) becomes negative immediately after breaking, with values one order of magnitude larger than the other two components of vorticity. The general pattern of vorticity changes significantly during the breaking wave evolution, with significant variation also in the vertical.

[Fig. 8abc](#) depicts the local derivative of the three components of vorticity (term  $I_v$  in eq. (7)). During breaking, the cross-shore vorticity components experience a local derivative spatially modulated in the vertical column and with alternating sign, with a pattern typical of instabilities (see [Fig. 8a](#) phases 1–4). The vertical vorticity ([Fig. 8b](#)) has a negative local derivative in most of the vertical column during phases 1–2 and then alternates sign in the subsequent phases. The alongshore vorticity ([Fig. 8c](#)) has a negative local derivative in most of the vertical column immediately after breaking (phase 2), and oscillates in the subsequent phases, being almost one order of magnitude larger than the other two components. However, the positive local derivative only reduces the magnitude of the negative alongshore vorticity but is not strong and persistent enough to turn it to positive values (see [Fig. 7d](#)). [Fig. 8d](#)

contains the values integrated in the vertical and shows the dominance of the alongshore vorticity component local derivative during the wave cycle.

In [Fig. 9](#), the advective terms of vorticity are shown. The contribution for the three components is comparable to the intrinsic time variations shown in [Fig. 8](#). Immediately after breaking the advection of the cross-shore vorticity is spatially modulated in the vertical column (see [Fig. 9a](#), phases 1–3) but with a small average value. Also, the advection of the vertical vorticity is spatially modulated in the vertical column (see [Fig. 9b](#), phases 1–3), but its average value is positive. The advection of the alongshore vorticity is almost everywhere negative, but a strong advection at  $\zeta \approx -0.4$  renders positive the average value in the vertical after breaking (see [Fig. 9c](#), phase 2), with several further oscillations in the subsequent phases (see [Fig. 9d](#)).

The third term in eq. (7) is analogous to the Reynolds stress term in the equation for the average flow field (see [Clavero et al., 2016](#)) and is associated with the mean transport of the fluctuating vorticity due to the fluctuating velocity. It is the divergence of a flux, i.e., a transport term. [Fig. 10abc](#) shows the phase-resolved distribution of the three components. Based on the phase-resolved values integrated in the vertical column ([Fig. 10d](#)), the term  $III_v$  is generally positive for the cross-shore (with a main contribution of the fluxes in the  $x$  and  $z$  directions, not shown) and the vertical components (with a main contribution of the fluxes in the  $x$  and  $y$  directions, not shown) except across breaking phases (phases 1–2). It is always negative for the alongshore component (with a main contribution of the fluxes in the  $x$  direction, not shown) and acts by increasing the intensity of the (negative)  $z$  component of vorticity.

[Fig. 11abc](#) shows the phase resolved distribution of the stretching term due to the interaction between the fluctuating vorticity and the fluctuating rate of strain tensor (term  $IV_v$  in eq. (7)). In the cross-shore direction, it assumes both positive and negative values with

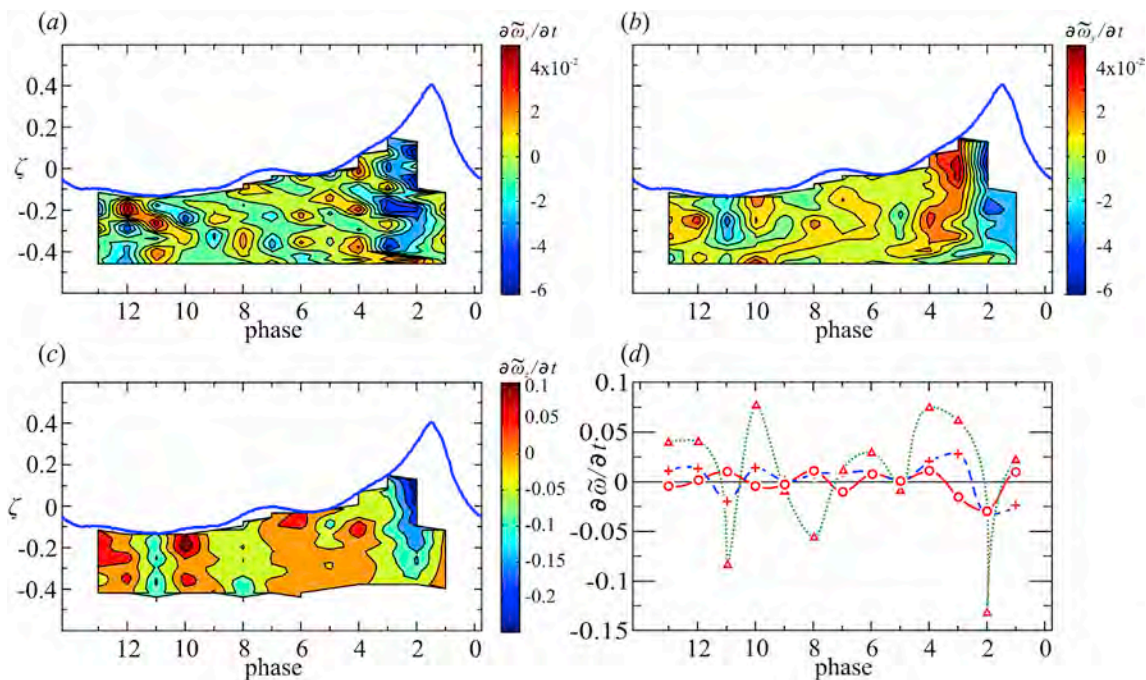


**Fig. 8.** Experiment 9b. Intrinsic time variation of the vorticity (term  $I_v$  in eq. (7)) (a) for the cross-shore vorticity, (b) for the vertical vorticity, and (c) for the alongshore vorticity as a function of  $\zeta = (y - \bar{\eta}) / (d + \bar{\eta})$ . (d) Mean values in the vertical of the cross-shore (circles), vertical (crosses), and alongshore (triangles) intrinsic time variation of vorticity. The intrinsic time variation of vorticity is normalized by  $(\partial \bar{\omega} / \partial t)(d + \bar{\eta})/g$ .

positive and negative peaks during breaking and during flow reversal (phase 12), respectively. The fluxes in the three directions (not shown) are of comparable magnitude. In the vertical direction, it reaches a negative minimum value immediately after breaking

(phase 2) and then oscillates around zero, with significant contribution of the fluxes in the  $x$  and  $y$  directions (not shown). In the alongshore direction, it is generally negative and acts similar to the term  $III_v$ , i.e., it enhances the negative  $z$  component of vorticity. It is

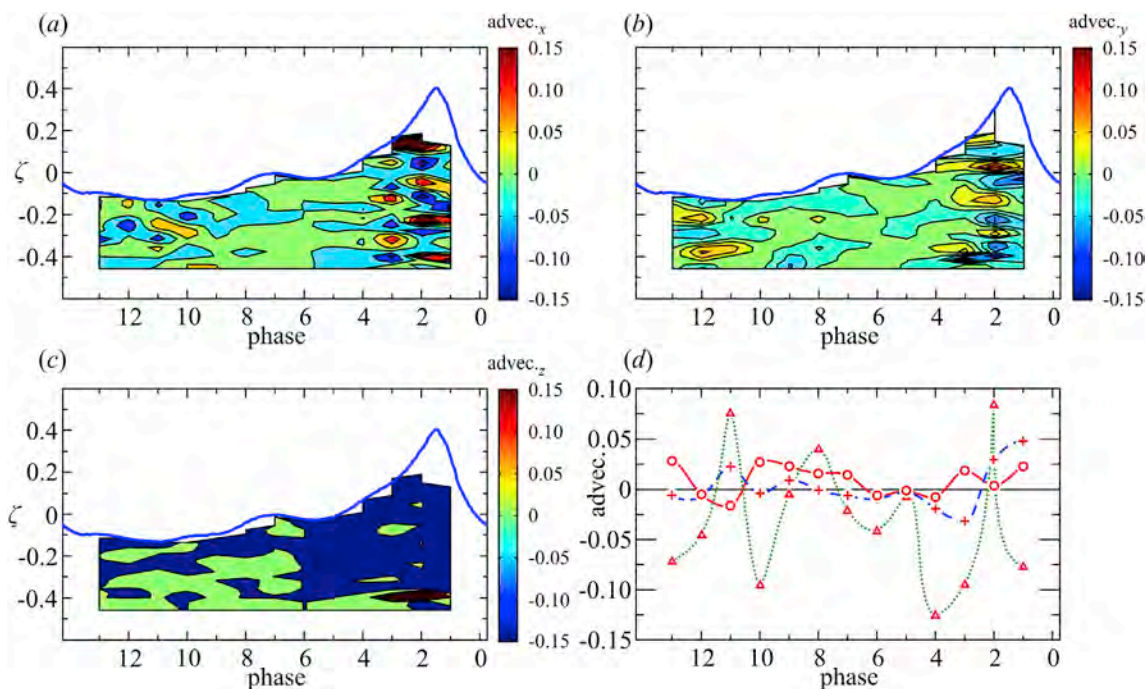


**Fig. 9.** Experiment 9b. Phase resolved advection (term  $II_v$  in eq. (7)) (a) for the cross-shore vorticity, (b) for the vertical vorticity, and (c) for the alongshore vorticity as a function of  $\zeta = (y - \bar{\eta}) / (d + \bar{\eta})$ . (d) Mean values in the vertical of the cross-shore (circles), vertical (crosses), and alongshore (triangles) advection of vorticity. The advection term is normalized by  $\bar{u}(\partial \bar{\omega} / \partial x)(d + \bar{\eta})/g$ .

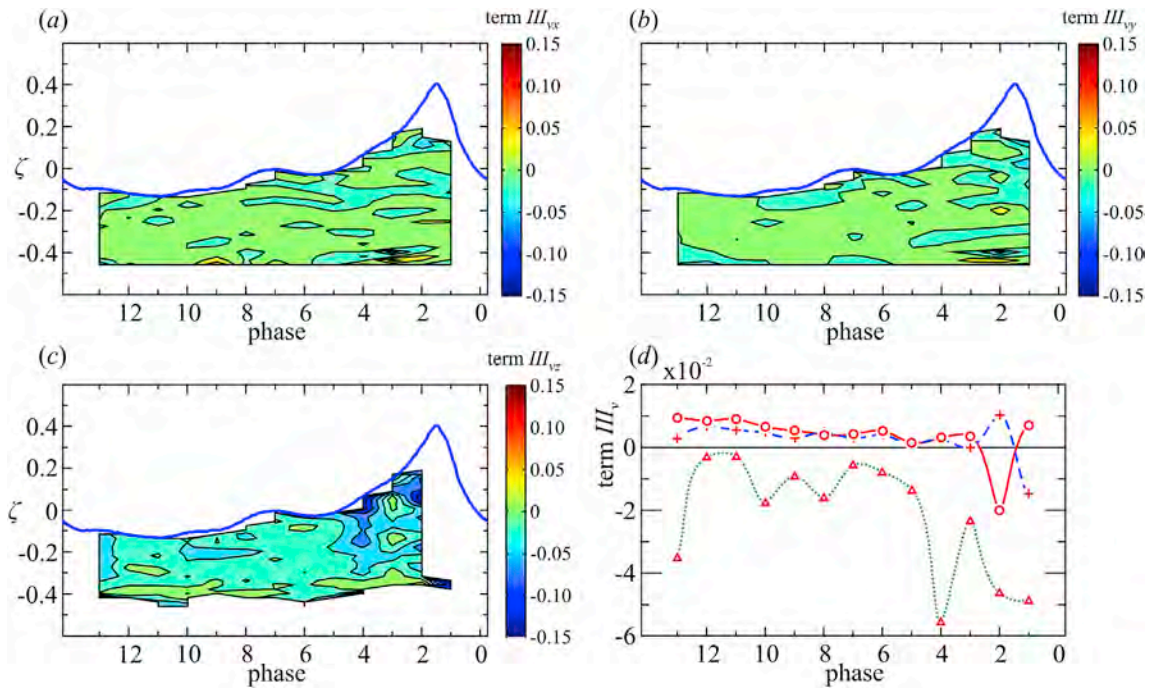


Fig. 10. Experiment 9b. Phase resolved mean transport of fluctuating vorticity due to turbulence (term  $III_v$  in eq. (7)) (a) for the cross-shore, (b) for the vertical, and (c) for the alongshore direction as a function of  $\zeta = (y - \bar{\eta}) / (d + \bar{\eta})$ . (d) Mean values in the vertical of the cross-shore (circles), vertical (crosses), and alongshore (triangles) components of term  $III_v$ . The term is normalized by  $(\partial(u_j \omega_i) / \partial x_j) (d + \bar{\eta}) / g$ .

mainly due to the flux in the  $z$  direction, except during reverse flow, during which the flux in the  $y$  direction becomes relevant (not shown).

The last significant term of eq. (7) is the stretching term due to the

interaction between the average vorticity and the rate of strain tensor of the average velocity (term  $V_v$ ) because viscous dissipation (term  $VI_v$ ) produces a negligible contribution and is not analysed. Fig. 12a depicts the various patterns of stretching for the cross-shore vorticity, with

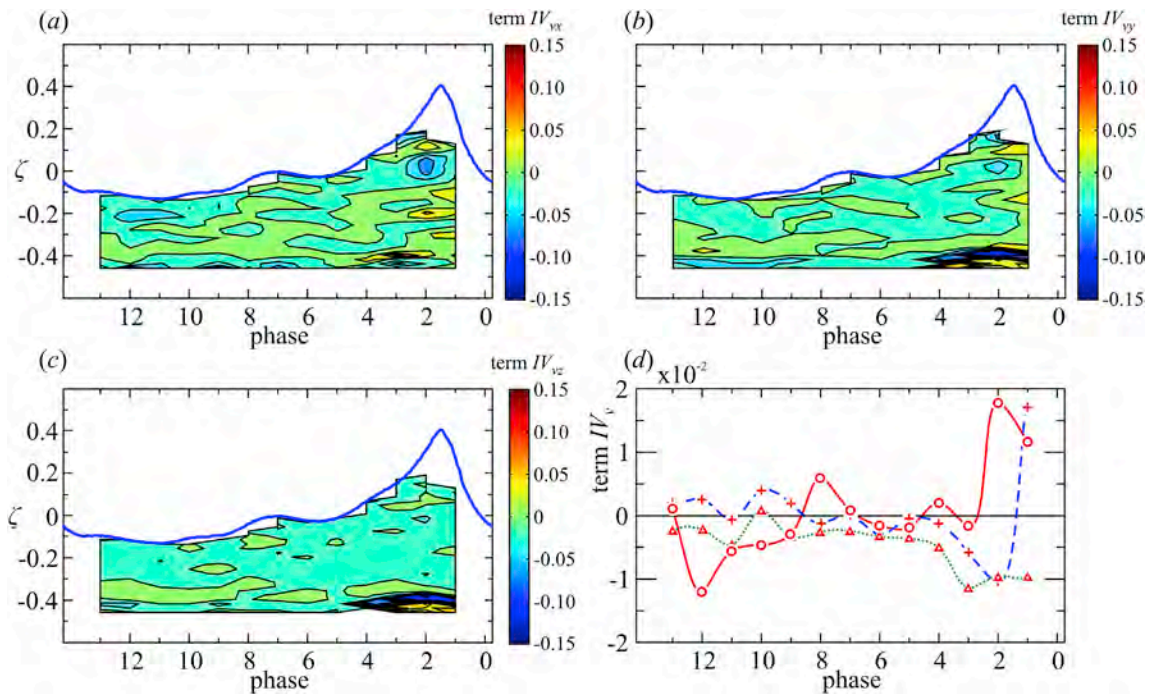


Fig. 11. Experiment 9b. Phase resolved stretching due to the fluctuating components (term  $IV_v$  in eq. (7)) (a) for the cross-shore direction, (b) for the vertical direction, and (c) for the alongshore direction as a function of  $\zeta = (y - \bar{\eta}) / (d + \bar{\eta})$ . (d) Mean values in the vertical of the cross-shore (circles), vertical (crosses), and alongshore (triangles) components. The term is normalized by  $(\omega_j \bar{S}_{ij}) (d + \bar{\eta}) / g$ .

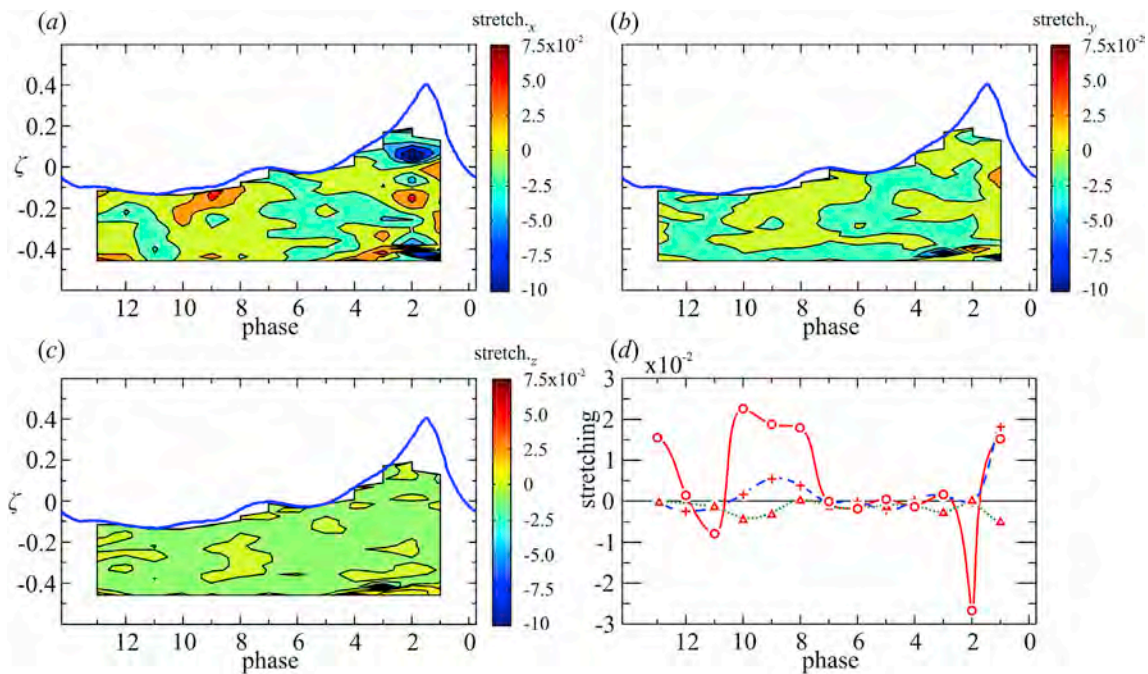


Fig. 12. Experiment 9b. Phase resolved stretching due to the average flow field (term  $V_v$  in eq. (7)) (a) for the cross-shore direction, (b) for the vertical direction, and (c) for the alongshore direction as a function of  $\zeta = (y - \bar{y}) / (d + \bar{\eta})$ . (d) Mean values in the vertical of the cross-shore (circles), vertical (crosses), and alongshore (triangles) stretching term. The stretching term is normalized by  $(\bar{\omega}_j \bar{S}_{ij})(d + \bar{\eta}) / g$ .

different zones of alternating sign in the vertical direction and in different phases. Fig. 12bc shows the distribution for the two other directions. Fig. 12d shows the values integrated in the vertical. The term in the cross-shore direction (x direction) is dominant and shows three peaks. One peak is negative and corresponds to the post-breaking phase (phase 2), and the other two are positive and occur during the flow reversal phases and immediately before breaking (phase 1). The vertical stretching is mainly positive and is limited to the post-breaking and flow reversal phases. The alongshore stretching is generally negative and of minor importance.

The balance of the three scalar vorticity equations is shown in Fig. 13abc. In the cross-shore direction (Fig. 13a) in the post-breaking phase (phase 2), the total variation of  $\bar{\omega}_x$  (term  $I_v + II_v$ ) is negative and all terms are of the same order of magnitude but with a positive stretching due to fluctuating velocity (term  $IV_v$ ). During flow reversal, the total variation of the alongshore vorticity is positive, and again the term  $IV_v$  is of opposite sign. The balance in the vertical direction (Fig. 13b) shows that the total variation of  $\bar{\omega}_y$  has two peaks in the breaking phase and during flow reversal. The main terms are due to turbulence (terms  $III_v$  and  $IV_v$ ) in the breaking phase, with a contribution of the average flow field (stretching term  $V_v$ ) in the flow reversal. The balance in the alongshore direction (Fig. 13c) is dominated by the transport due to turbulence (term  $III_v$ ). The most important variations in vorticity are in the alongshore and cross-shore directions; the vertical direction is of minor importance.

We cannot state the equivalence between vorticity and vortices because a high vorticity level is recorded in association with the presence of vortices and the presence of shear layers. However, the results of the present experiments indicate that the sequence of horizontal (alongshore) and streamwise (cross-shore) vortices detailed by, for example, in Watanabe et al. (2005), is compatible with the experimental vorticity dynamics. Although only a portion of the vertical column is in the FOV of the V3V (the near-bottom region and the crest are not in the volume of

measurement), the overall balance of the average vorticity is unexpectedly almost satisfied for the three directions, with minor discrepancies in the breaking phases.

#### 4.3. A comparison of vorticity in similar conditions without berm

A set of experiments which shares many similarities with the present experiments is detailed in Kimmoun and Branger, (2007), where planar PIV is used to reconstruct the flow field of waves breaking on a 1:15 beach in a flume. They tested waves with breaker of the spilling type, with period  $T = 1.275$  s and surf-similarity parameter equal to 0.28. The non dimensional vorticity has a maximum after breaking and is one order of magnitude larger than the vorticity recorded in the present experiments, with values up to  $\approx 3.4$ . Strong differences are evident also by comparing the mean vorticity in the vertical in Fig. 4 of Longo (2003), which shows a maximum of  $20 \text{ s}^{-1}$  ( $\approx 2.2$  in non dimensional value) and is negligible below the trough. The numerical simulations by Christensen and Deigaard (2001) indicate a very high value of topologically induced vorticity for a weak plunger (Fig. 9 in that paper, mid panel, shows iso-vorticity lines with values up to  $50 \text{ s}^{-1}$ ,  $\approx 8.7$  in non dimensional value). Many other experiments (e.g., Nadaoka et al., 1989) report a mean vorticity of  $O(10 \text{ s}^{-1})$ , which in dimensionless values is still higher than the mean (alongshore-)vorticity of the present experiments. Essentially it seems that the presence of the submerged berm reduces the vorticity and favors the diffusion with respect to breakers without the berm.

A special comparison is available with the experiments by Petti et al. (1994), where a submerged berm was on a 1:100 inclined beach. Petti et al. with the aid of a planar PIV found again values of vorticity of  $O(10 \text{ s}^{-1})$ , much larger than the vorticity measured in the present experiments. A possible explanation of the differences is the different beach inclination (we recall that in the present experiments we have a 1:10

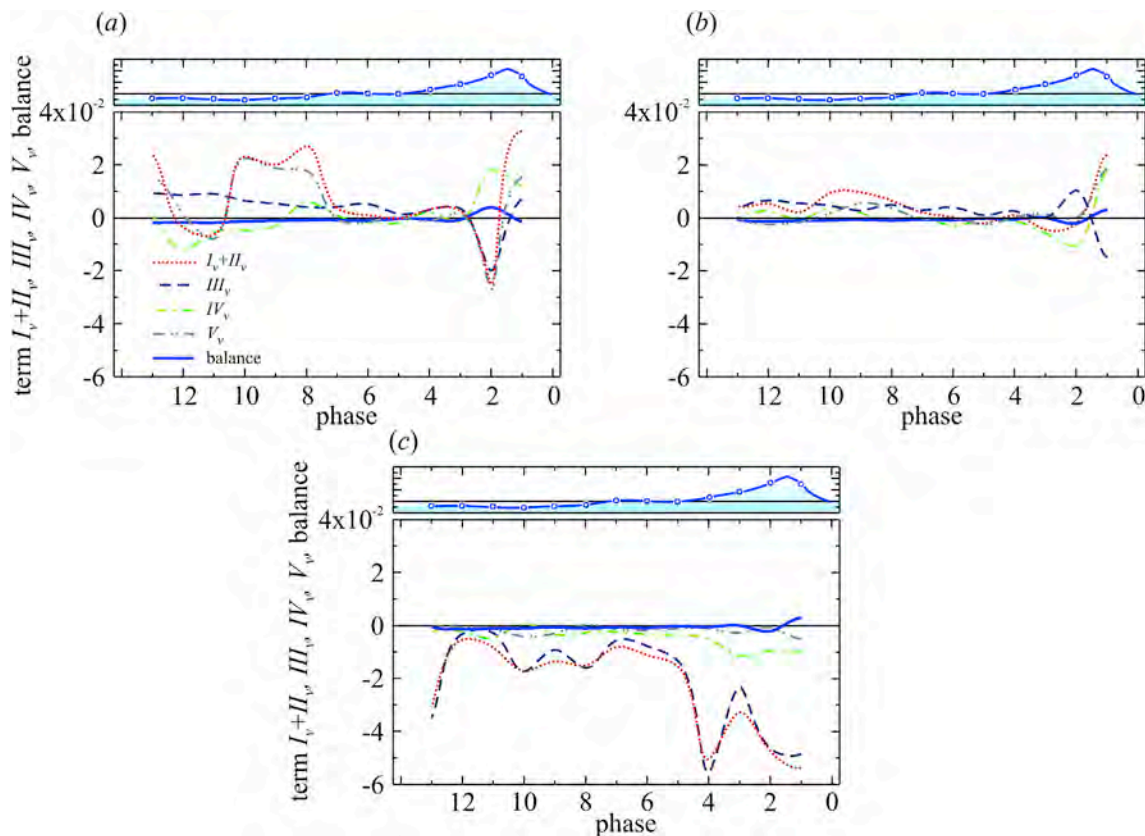


Fig. 13. Experiment 9b. Phase resolved balance of vorticity (a) for the cross-shore vorticity, (b) for the vertical vorticity, and (c) for the alongshore vorticity at different phases. The material derivative (sum of the intrinsic time variation and of the advection) (dotted red line), term  $III_v$ , in eq. (7) (dashed line), the vortex stretching due to fluctuating velocities (dash-dot line), the vortex stretching due to the average flow (dash-dot-dot line), and the balance defect (solid line) are shown. The upper sub panels indicate the phase resolved surface elevation. (For interpretation of the references to colour in this figure legend, the reader is referred to the web version of this article.)

bottom inclination), which reduces the swash and constrains vortices and eddies much more in the present experiments than in Petti et al. experiments. The intense coexistence of eddies favors their interaction and the stretching process and results in a faster decay of vorticity toward scales smaller than the detectable scales.

### 5. A possible mechanism for vortex generation at the free surface

In addition to the numerous sources of eddies and coherent structures already listed in §4.1, a new mechanism is observed in the present experiments. Fig. 14 shows a different mechanism for direct generation of vorticity, possibly evolving in counter-rotating eddies with axes aligned cross-shore. The non-uniform (in the alongshore direction) breaking crest injects momentum with major components in the cross-shore and vertical directions and with a maximum in the mid-section. The strong shear in the vertical planes increases the vorticity and facilitates the generation of two counter-rotating vortices with cross-shore axes. Essentially, this generation can be attributed to the finite size of the breaking wave front, which is created in the flume by the wall boundary layers (a source of vortices with vertical axis) but is also expected to appear in the field as a consequence of short-crested waves and the alongshore variability in the breaking crest. Furthermore it should appear in numerical codes which work with lateral zero flow conditions to limit the numerical spatial domain. These cross-shore axis vortices should appear jointly with the vertical axis vortices already described at the end of the breaking wave crest. This

observation must be considered with care and there are numerous caveats which prevent firm conclusions. First of all the flume limits the alongshore geometry of the coherent structures, which in the field can be much important and relevant. Undertow is somehow constrained and no longshore currents or edge waves develop. The presence of the bar itself is a barrier to cross-shore eddies, which cannot travel offshore and accumulate beneath the free surface and affect the flow field. The friction due to vertical walls generates additional shear in the vertical-cross-shore planes and favors higher speed in the midsection of the flume. A way to check the effect of the vertical walls is to artificially increase their roughness and to observe the overall effects. Essentially, this mechanism for vortex generation could be a laboratory effect and an experimental confirmation in the field is requested for a firm conclusions.

### 6. Conclusions

The analysis of the mean vorticity highlights the variable and difficult-to-model complexity of the flow field. Vorticity coexists with a wave flow (in principle a potential flow) and evolves to fill the domain with vorticity associated with shear or coherent structures. The vortices, either with an alongshore axis or with a diagonal axis in the cross-shore-vertical planes, and the vorticity tubes with a tortuous paths have been detected by visual observation and velocity measurement analysis, respectively. The vortical tubes behave like vortical tubes in other complex flow fields and reveal a variety of mutual interactions that can be

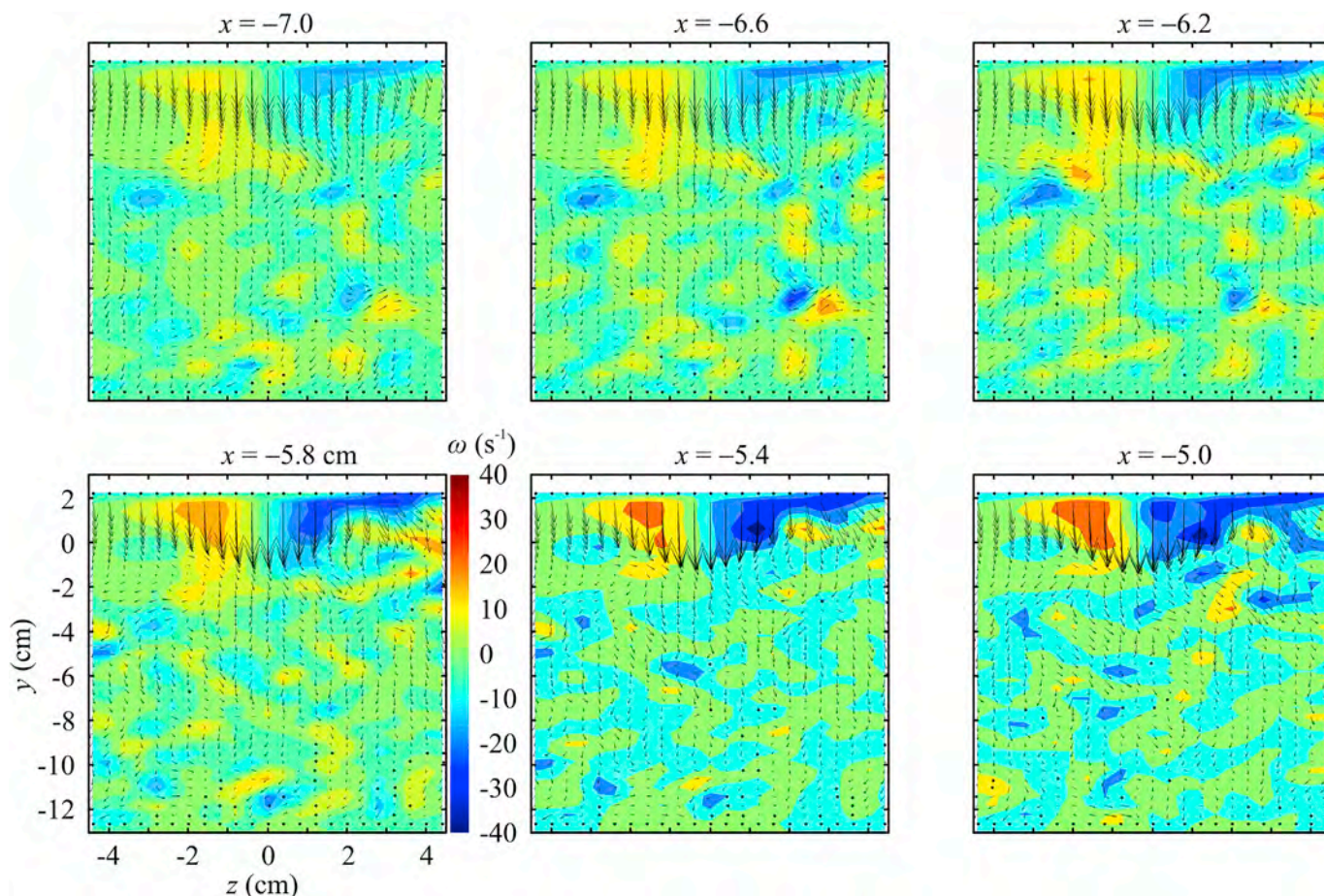


Fig. 14. Experiment 5b, phase 2, wave cycle 8. Instantaneous turbulent velocity field and vorticity contours shown in alongshore-vertical planes ( $z$ - $y$ ) at various cross-shore locations, with a space step equal to 0.4 cm.

referred to transition phenomena.

The main component of vorticity is directed alongshore. The temporal evolution of vorticity in the cross-shore direction is controlled by vortex stretching due to the average flow, especially during flow reversal. In the breaking phase, vortex stretching is also associated with the fluctuating strain rate and the flux of fluctuating vorticity due to turbulence. In the alongshore direction, the balance is mainly due to the flux of fluctuating vorticity due to turbulence; other terms are less relevant. In the vertical direction, all the terms show the same magnitude.

The measured values of vorticity are generally smaller than the values in absence of the submerged berm documented in other experiments. The topologically induced vorticity concentrated near the free surface is reduced in favor of a more uniform vorticity in the water column. It is also forecast that the geometric constraint represented by the berm (in the offshore direction) and by the beach (a 1:10 beach reduces the swash zone and confines the flow domain) favors the interaction amongst the vortices with a consequent fast transfer toward small scale vortices, non detectable with the spatial resolution of the V3V system.

A new possible mechanism of generation of vorticity has been detected and is triggered by the wall boundary layers in the lab flumes. In the field, this process may be associated with the finite crest length and alongshore variations in the flow field (in this respect, the sources are similar to the sources of large scale eddies with vertical axis). However, the numerous constraints due to the flume geometry suggest caution in transferring these results to field results. Indirect indications can be gained with experiments in a flume with artificially increase

roughness of the vertical walls, numerical computations with bounded spatial domain. More direct indications could be gained with 3D wave tank experiments similar to the experiments by Haller et al. (2002) or field experiments.

The present analysis with richness of details and with the direct evaluation of numerous terms in vorticity balance confirm the power of a three dimensional measuring system. The spatial resolution (0.4 cm) and the size of the volume of measurements ( $10 \times 10 \times 14 \text{ cm}^3$ ), with also a limited data rate (7.25 Hz), do not represent serious obstacles for a deep insight in the most subtle mechanisms behind vorticity dynamics and, in general, behind breaking waves dynamics. Indeed new graphic tools for data visualization and interpretation are required in view of forthcoming systems with improved space and time resolutions. The availability of a huge amount of data forces to better conceived conceptual models in order to recap the information.

### Appendix A

Figure Appendix A.1 shows the instantaneous velocity for Experiment 6b, fourth phase, first wave cycle. The panels are 0.8 cm space apart. Figure Appendix A.2 shows the three components of the instantaneous vorticity for Experiment 6b, fourth phase, first wave cycle.



Figure Appendix A.1. Instantaneous velocity vectors (only cross-shore and vertical components) for Experiment 6b, fourth phase, first wave cycle.

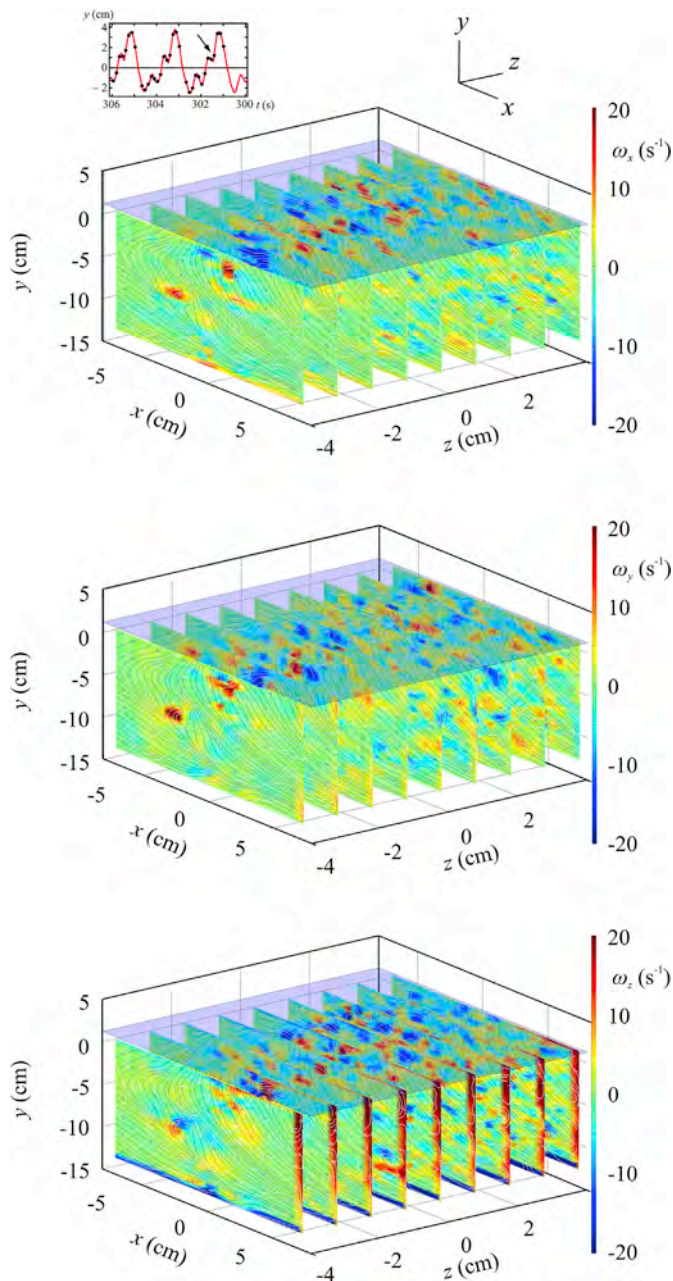


**Figure Appendix A.2.** Instantaneous vorticity components for Experiment 6b, fourth phase, first wave cycle, (a) x component, (b) y component, and (c) z component. The streamlines refer to velocity (blue curves) and to vorticity (white thick curves).

## References

- Baldock, T., 2006. Long wave generation by the shoaling and breaking of transient wave groups on a beach. *Proc. R. Soc. Lond. A Math. Phys. Eng. Sci.* 462 (2070), 1853–1876. <http://dx.doi.org/10.1098/rspa.2005.1642>.
- Baldock, T.E., O'Hare, T.J., Huntley, D.A., 2004. Long wave forcing on a barred beach. *J. Fluid Mech.* 503, 321–343. <http://dx.doi.org/10.1017/S002211200400792X>.
- Bühler, O., 2000. On the vorticity transport due to dissipating or breaking waves in shallow-water flow. *J. Fluid Mech.* 407, 235–263. <http://dx.doi.org/10.1017/S0022112099007508>.
- Calderon, D.E., Wang, Z., Gursul, I., 2012. Three-dimensional measurements of vortex breakdown. *Exp. Fluids* 53 (1), 293–299. <http://dx.doi.org/10.1007/s00348-012-1317-1>.
- Chang, K.-A., Liu, P.-F., 1998. Velocity, acceleration and vorticity under a breaking wave. *Phys. Fluids* 10 (1), 327–329. <http://dx.doi.org/10.1063/1.869544>.
- Christensen, E., Deigaard, R., 2001. Large eddy simulation of breaking waves. *Coast. Eng.* 42 (1), 53–86. [http://dx.doi.org/10.1016/S0378-3839\(00\)00049-1](http://dx.doi.org/10.1016/S0378-3839(00)00049-1).
- Clavero, M., Longo, S., Chiapponi, L., Losada, M., 2016. 3D flow measurements in regular breaking waves past a fixed submerged bar on an impermeable plane slope. *J. Fluid Mech.* 802, 490–527. <http://dx.doi.org/10.1017/jfm.2016.483>.
- Dabiri, D., Gharib, M., 1997. Experimental investigation of the vorticity generation within a spilling water wave. *J. Fluid Mech.* 330, 113–139. <http://dx.doi.org/10.1017/S0022112096003692>.
- Derakhti, M., Kirby, J., 2014. Bubble entrainment and liquid–bubble interaction under unsteady breaking waves. *J. Fluid Mech.* 761, 464–506. <http://dx.doi.org/10.1017/jfm.2014.637>.
- Fritts, D.C., Arends, S., Andreassen, Ø., 1998. Vorticity dynamics in a breaking internal gravity wave. Part 2. Vortex interactions and transition to turbulence. *J. Fluid Mech.* 367, 47–65. <http://dx.doi.org/10.1017/S0022112098001633>.
- Haller, M.C., Dalrymple, R.A., Svendsen, I., 2002. Experimental study of near shore dynamics on a barred beach with rip channels. *J. Geophys. Res. Oceans* 107 (C6). <http://dx.doi.org/10.1029/2001JC000955>, 14–1–14–21.
- Holton, J.R., Haynes, P.H., McIntyre, M.E., Douglass, A.R., Rood, R.B., Pfister, L., 1995. Stratosphere-troposphere exchange. *Rev. Geophys.* 33 (4), 403–439. <http://dx.doi.org/10.1029/95RG02097>.
- Kimmoun, O., Branger, H., 2007. A particle image velocimetry investigation on laboratory surf-zone breaking waves over a sloping beach. *J. Fluid Mech.* 588, 353–397. <http://dx.doi.org/10.1017/S0022112007007641>.
- Kowalczyk, A., Szlachta, A., Hanus, R., 2012. Standard uncertainty determination of the mean for correlated data using conditional averaging. *Metrol. Meas. Syst.* 19 (4), 787–796.
- Li, L., Dalrymple, R., 1998. Instabilities of the undertow. *J. Fluid Mech.* 369, 175–190.
- Lin, P., Liu, P.-F., 1998. Turbulence transport, vorticity dynamics, and solute mixing under plunging breaking waves in surf zone. *J. Geophys. Res.* 103 (C8), 15677–15694.
- Lin, J., Rockwell, D., 1994. Instantaneous structure of a breaking wave. *Phys. Fluids* 6 (9), 2877–2879. <http://dx.doi.org/10.1063/1.868113>.
- Longo, S., 2003. Turbulence under spilling breakers using discrete wavelets. *Exp. Fluids* 34 (2), 181–191. <http://dx.doi.org/10.1007/s00348-002-0545-1>.
- Longo, S., Petti, M., Losada, I., 2002. Turbulence in the swash and surf zones: a review. *Coast. Eng.* 45 (34), 129–147. [http://dx.doi.org/10.1016/S0378-3839\(02\)00031-5](http://dx.doi.org/10.1016/S0378-3839(02)00031-5).
- Longo, S., Chiapponi, L., Clavero, M., 2014. Experimental analysis of the coherent structures and turbulence past a hydrofoil in stalling condition beneath a water–air interface. *Eur. J. Mechanics-B/Fluids* 43, 172–182. <http://dx.doi.org/10.1016/j.euromechflu.2013.08.007>.
- Longuet-Higgins, M., 1992. Capillary rollers and bores. *J. Fluid Mech.* 240, 659–679. <http://dx.doi.org/10.1017/S0022112092000259>.
- Nadaoka, K., Hino, M., Koyano, Y., 1989. Structure of the turbulent flow field under breaking waves in the surf zone. *J. Fluid Mech.* 204, 359–387. <http://dx.doi.org/10.1017/S0022112089001783>.
- Ohm, K., Li, H.Y., 2000. Particle-tracking velocimetry with new algorithms. *Meas. Sci. Technol.* 11 (6), 603.
- Peregrine, D.H., 1998. Surf zone currents. *Theor. Comput. Fluid Dyn.* 10 (1–4), 295–309.
- Petti, M., Quinn, P., Liberatore, G., Easson, W., 1994. Wave velocity field measurements over a submerged breakwater. *Coast. Eng.* 1995, 525–539.
- Raffel, M., Willert, C.E., Wereley, S., Kompenhans, J., 2013. *Particle Image Velocimetry: a Practical Guide*. Springer.
- Roelvink, J.A., Stive, M.J.F., 1989. Bar-generating cross-shore flow mechanisms on a beach. *J. Geophys. Res. Oceans* 94 (C4), 4785–4800. <http://dx.doi.org/10.1029/JC094iC04p04785>.
- Sharp, K., Hill, D., Troolin, D., Walters, G., Lai, W., 2010. Volumetric three-component velocimetry measurements of the turbulent flow around a Rushton turbine. *Exp. Fluids* 48 (1), 167–183. <http://dx.doi.org/10.1007/s00348-009-0711-9>.
- Tennekes, H., Lumley, J., 1972. *A First Course in Turbulence*. Cambridge University Press.
- Ting, F., Reimnitz, J., 2015. Volumetric velocity measurements of turbulent coherent structures induced by plunging regular waves. *Coast. Eng.* 104, 93–112. <http://dx.doi.org/10.1016/j.coastaleng.2015.07.002>.
- Watanabe, Y., Saeki, H., Hosking, R., 2005. Three-dimensional vortex structures under breaking waves. *J. Fluid Mech.* 545, 291–328. <http://dx.doi.org/10.1017/S0022112005006774>.
- Yeh, H.H., 1991. Vorticity-generation mechanisms in bores. *Proc. Royal Soc. Lond. A Math. Phys. Eng. Sci.* 432 (1885), 215–231. <http://dx.doi.org/10.1098/rspa.1991.0014>.
- Zhang, D., Sunamura, T., 1994. Multiple bar formation by breaker-induced vortices: a laboratory approach. *Coast. Eng.* 1995, 2856–2870. <http://dx.doi.org/10.1061/9780784400890.207>.